PRAMANA
— journal of
physics

Vol. 75, No. 5
November 2010
pp. 837–854

Absorption and dispersion in metamaterials: Feasibility of device applications

SUBIMAL DEB and S DUTTA GUPTA*
School of Physics, University of Hyderabad, Hyderabad 500 046, India
*Corresponding author. E-mail: sdghyderabad@gmail.com; sdgsp@uohyd.ernet.in

Abstract. We present a quantitative study of the effects of losses in layered media with a metamaterial layer as the constituent. The metamaterial is modelled by a causal isotropic effective medium (Lorentz-type) response. The parameters for the model are picked from a recent experiment. Two specific examples, namely, that of resonant tunnelling (RT) and imaging are chosen to demonstrate the devastating effects of losses in the present day metamaterials. It is then shown how large delays in RT, as well as near perfect imaging can be restored in gain-doped metamaterials. We also point out yet another use of metamaterials for achieving near perfect absorption, and its use for probing strong atom–field interaction.

Keywords. Metamaterials; resonant tunnelling; group delay; perfect imaging; perfect absorption.

PACS Nos 78.67.Pt; 42.70.-a; 42.25.Bs

1. Introduction

In recent years there has been a great deal of interest in negative index materials (NIMs) because of their exotic physical properties and potential applications. Historically, the possibility of having negative refractive index, and consequently counterintuitive physical effects were first pointed out by Veselago [1]. It was shown that the standard Maxwellian electrodynamics holds for simultaneously negative permittivity (ϵ) and permeability (μ), with interesting consequences of negative refraction, negative Doppler shift, negative Cherenkov radiation, etc. Evidently such materials do not occur in nature and the possible route to realize them was explored by Sir John Pendry, who showed that a finite magnetic response can be extracted from non-magnetic materials [2]. In fact he proposed the split-ring resonator (SRR) and swiss roll structures to achieve negative permeability [2,3]. Negative permittivity was not a major problem (albeit at lower frequencies) since metals are known to possess large negative real part over large frequency ranges. Pendry's discovery of a perfect lens the very next year served as a real impetus for opening the floodgates for metamaterial (MM) research. Pendry elaborated on Veselago's proposal of lensing (due to negative refraction) to show that a slab of negative material

can amplify the evanescent waves. Thus in contrast to the usual lens (which collects only the propagating part) the Pendry lens was 'perfect'. Combined with the knowledge and advances of near-field optics, the tremendous possibilities of such a lens for super-resolution (beyond the Rayleigh limit) were immediately understood. Experiments on MMs were not lagging too far behind. In 2000 itself MMs in the microwave domain were reported [4]. The experimental realization of MMs in higher frequency domain exploiting various structures (SRR, fish-net, etc.) are now routinely reported [5]. The goal is to achieve negative refraction at higher and higher frequencies with lower losses, resulting in higher FOM ($|\mathrm{Re}(n)/\mathrm{Im}(n)|$, where n is the refractive index). There are now extensive and well-written reviews [3,5,6] which highlight both the theoretical and experimental achievements over the past decade. They also focus on the exotic applications of MMs which range from super-lensing and super-resolution (SR) [7,8] to lasing spasers [9] and optical nanocircuits [10]; invisibility cloaks to electromagnetically-induced transparency and slow or stopped light [11,12], etc. The field has grown so much that there is a need to understand what one understands under MMs. One of the recent books defines them as 'artificial effectively homogeneous electromagnetic structures with unusual properties not readily available in nature' [13]. In this article we restrict ourselves to the classical notion of MMs as negative index materials or left-handed materials as discussed by Veselago, where both ϵ and μ are negative, though in the last section we use the term MMs to describe artificial materials with $\mu > 0$, $\epsilon < 0$.

In most of the current MMs negative refraction is accompanied by substantial losses, more so at higher frequencies. The origin of these losses can be traced to the fact that refractive index becomes negative close to electromagnetic resonances where the absorption is high. Presence of large absorption is associated with large dispersion via the Kramers–Kronig relations. In MMs at lower frequencies such strong dispersion was exploited to show the feasibility of slow light [11]. Achieving large delays in the higher frequency range can thus pose a challenging problem. In an analogous fashion, achieving desired SR at higher frequencies is also threatened by high losses. In this paper we concentrate on two specific examples, the delay devices and MM lens, in order to make a quantitative assessment of the effects of losses. We use the parameters of a recently reported MM [14] by fitting the experimental data for the permeability to a causal Lorentz-type model, whereas we use the interpolated experimental data for the permittivity.

For delay studies we use a resonant tunnelling (RT) configuration, whereby a guiding structure is embedded in between two high index prisms and two spacer layers on each side. Of late, there has been a great deal of interest in such tunnelling structures both for fundamental studies and for applications. It is clear that (beyond certain critical angle of incidence) because of evanescent waves in the spacer layers, light is not transmitted through it unless the modes of the guides are excited. In narrow bands of angles (for fixed frequency) or frequencies (for fixed angles) there can be RT, associated with large dispersion resulting in large delays. We calculate the delay or the Wigner phase time [15], as the frequency derivative of the phase of the transmission coefficient. For testing the lensing and SR effects we use the usual Pendry lens configuration. We show that the damping as in the available materials at near-infrared and visible frequencies can have devastating effects on both RT and SR.

It is thus essential to find a way out to reduce the losses at least at and near the working frequency. The obvious route is to introduce gain in the MM. Based on a detailed analysis of the Kramers–Kronig relations it was claimed that passive MMs need to be lossy in order to possess negative refraction [16]. It was further argued that even with gain there is a lower bound to the losses and there cannot be truly non-lossy MMs. Later it was shown that the latter conclusion is not correct. In fact, the losses can be minimized to zero by digging a hole in the absorption profile. Local reduction of losses in the frequency domain does not violate causality [17]. In this paper we work with such a model where increasing gain can reduce the effective absorption ($\mathrm{Im}(n)$) to near-zero at a specified frequency. We demonstrate how the RT features and the associated large delays can be recovered. In the context of Pendry lensing we demonstrate how subwavelength imaging can be restored. In fact one of the major directions in current MMs research is the theoretical and experimental feasibility of making them lossless [18–23].

Passive MMs, though lossy, can have interesting applications albeit in a different frequency domain, where $\mu > 0$ but $\epsilon < 0$. The transmission through a slab of such MM exhibits a band gap much like in one-dimensional periodic structures [24]. A dielectric cavity with mirrors formed by such MMs can exhibit critical coupling (CC), whereby, all the incident energy is absorbed by the walls of the cavity. Such a cavity does not allow the radiation to pass through, yet maintaining exceedingly low reflection. In other words, such a cavity acts like a near-perfect absorber at one or more frequencies. In this paper we briefly review the interaction of such a cavity with resonant atoms to show that strong atom–cavity interaction can lead to mode splitting like vacuum Rabi splittings in cavity QED [25–29].

The structure of the paper is as follows. In §2 we recall the essentials of treating layered media using a characteristic matrix formalism. We use the formalism to calculate the transmission through the structure and pulse delay. For the image problem we use the usual spatial harmonic decomposition to calculate the image profiles for objects with sub-wavelength details. Finally in the context of atom–field coupling, we study the poles of the amplitude reflection/transmission for the signature of the mode and the lifetime splittings. In §3 we show that absorption-compensation can indeed lead to a recovery of the RT feature and the associated large delay of the pulse. We consider both the plasmon-like and the guided modes. In §4 we look at the imaging aspects of a Pendry lens with MM as in [14]. We show how the flat features due to large absorption can be overcome by introducing gain leading to near-perfect imaging. Section 5 is devoted to critically coupled cavity with resonant atoms. We demonstrate how stronger coupling in denser medium can lead to well-separated CC dips. Finally in §6 we summarize the main results of this paper.

2. Characteristic matrix formalism

In this section we recall the characteristic matrix approach for obtaining the reflection and transmission features of a layered structure (figure 1). Let the structure be illuminated by a plane monochromatic wave at an angle θ_i. The amplitude reflection (r) and transmission (t) coefficients of such a structure are given by [30–32]

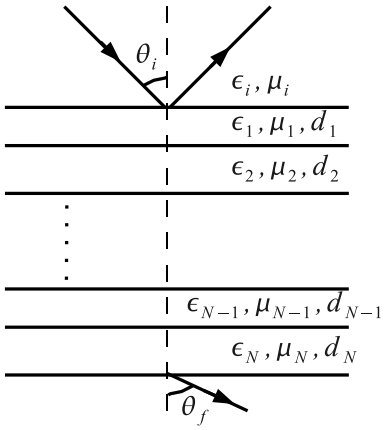

Figure 1. Schematic of a layered structure.

$$r = \frac{(m_{11} + m_{12}p_f)p_i - (m_{21} + m_{22}p_f)}{(m_{11} + m_{12}p_f)p_i + (m_{21} + m_{22}p_f)}$$

$$t = \frac{2p_i}{(m_{11} + m_{12}p_f)p_i + (m_{21} + m_{22}p_f)} \tag{1}$$

where m_{ij} $(i, j = 1, 2)$ are the elements of the total characteristic matrix of the structure (the expressions for m_{ij} $i, j = 1, 2$ can be found in [30]),

$$p_{i,f} = \begin{cases} \sqrt{\epsilon_{i,f}/\mu_{i,f}}\cos\theta_{i,f} & \text{(TE polarization)} \\ \sqrt{\mu_{i,f}/\epsilon_{i,f}}\cos\theta_{i,f} & \text{(TM polarization)} \end{cases} \tag{2}$$

and $\theta_{i,f}$ are the angles of incidence and emergence in the first and the last medium, respectively. The intensity reflection (R) and transmission (T) of the structure are given by $R = |r|^2$ and $T = |t|^2$ (for identical media of incidence and emergence). In the context of RT, the excited modes appear as sharp peaks in the transmission profile (as a function of the angle of incidence). To determine the delay characteristics of the structure, we extract the phase of the transmission coefficient. The frequency derivative of the phase of amplitude transmission then gives the Wigner delay through the structure [15]. Further, in the context of CC leading to complete absorption, one needs to consider the energy conservation condition given by $R + T + A = 1$ (A – absorption of the structure). As most of the incident energy goes in absorption, the total scattering $(R + T)$ of a critically coupled system must be near zero. Thus, for CC we mostly study the total scattering from the structure.

Note that a common denominator figures in the expressions of both the reflection and transmission coefficients (eq. (1)). The zeroes of the denominator bear the information about the characteristic frequencies (eigenmodes) of the system. The corresponding equation (also known as the dispersion equation) can be written as [32,33]

$$D = (m_{11} + m_{12}p_f)p_i + (m_{21} + m_{22}p_f) = 0. \tag{3}$$

The dispersion relation (3) can be solved only for complex frequencies, which carries all the information about the modes and their associated decay rates. In fact, the real part of the roots gives the locations of the modes, while the imaginary part corresponds to the width of these resonances. Due to the transcendental nature of eq. (3) it cannot be solved analytically. We revert to a numerical scheme to obtain the distinct branches for the split modes.

3. Resonant tunnelling through a metamaterial guide

The phenomenon of tunnelling of light has been known since the time of Newton [34]. When light is incident at an angle larger than the critical angle of a high-index prism–air interface, the incident plane wave suffers total internal reflection. However, the evanescent waves can penetrate into air and propagate if another high-index prism is placed close to the first one. This is analogous to the quantum mechanical tunnelling of electrons across a potential barrier [35]. As opposed to this, tunnelling through two barriers separated by a well describes the situation of resonant tunnelling [36]. The finite transmission through the barriers is mediated by the quasibound states of the well. The optical equivalent would be a waveguide separated from two high index prisms by a gap layer on either side (see figure 2). Here the RT is mediated by the guided and surface modes of the structure. RT of light has been studied theoretically and experimentally with alternating metal–dielectric layered systems with single as well as multiple metal layers [37–39]. RT has been reported in aluminium–dielectric multilayers demonstrating its potential for use, for example, for surface plasmon-mediated enhanced transmission [39]. The use of corrugated metal-photoresist layered structures as narrow-band filters at a

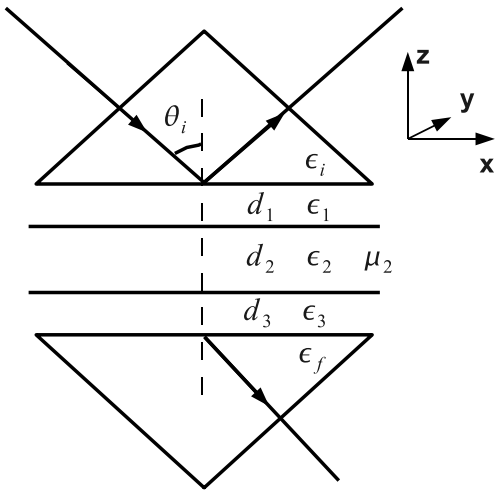

Figure 2. Schematic of the layered structure with central NIM layer sandwiched between two spacer layers and high index prisms. All materials except the NIM are assumed to be non-magnetic.

wavelength around 1500 nm was demonstrated in [38]. Dielectric-clad metal waveguide structures with interruptions in the metal guide were studied at a wavelength of 785 nm [40] to show that surface modes can also tunnel resonantly. Both symmetric and asymmetric configurations were reported to have high transmission efficiency across the interruptions. Moreover, these structures were shown to be robust to technical imperfections. Metal–dielectric structures have been studied recently in the context of slow light and enhanced transmission in a gap plasmon guide [41]. The enhanced transmission was mediated by the modes of a multilayered metal–dielectric structure. Thus RT geometries show interesting application potentials for optical signal processing and for integrated photonic systems.

The role of material dispersion in the transmission features of an NIM guide in the RT configuration was subsequently studied in [42]. Considering the full causal response, it was shown that the losses in the present-day MMs destroy the RT features. However, as magnetic losses are known to play a significant role in controlling the left-handed behaviour of MMs, the delay features could be recovered upon using an improved magnetic response. This motivates the choice of investigating the same RT structure with an absorption-compensated NIM guide. There have been extensive studies to obtain low-loss MMs or to compensate losses by gain. For example, a clever use of negative liquid crystals as a host renders MM properties dynamically controllable with ohmic losses compensated by gain in the inclusions [23]. Feasibility of similar negative permittivity with quantum dots was also discussed. Ideas of electromagnetically-induced transparency were ported to MM to reduce losses [20,21]. From a totally different angle, gaseous media like metastable Ne was proposed to achieve lossless negative refraction [19]. Here we use an MM doped with a magnetic gain material such that the absorption is near-zero locally (in the frequency domain). We shall show that such an NIM with absorption-compensating gain can not only aid the recovery of the transmission features of the RT structure but also give rise to very large time delays.

Let us consider the RT structure shown in figure 2 consisting of an NIM slab sandwiched between two non-magnetic dielectric layers and high-index prisms. The guided (plasmon-like) modes [43] of the structure can be excited when the magnitude of the refractive index of the NIM slab is higher (lower) than those of the surrounding dielectric slabs. We shall probe the transmission features mediated by both these modes and compare the time delays with and without suppression of absorption (at the working wavelength) in the NIM slab. Recall that the time delay of a pulse (at a carrier frequency ω_c) through a segment of length d is given by the frequency derivative of the phase of the transmission coefficient ($t = |t| \exp(i\phi_t)$):

$$\tau = \left.\frac{\partial \phi_t}{\partial \omega}\right|_{\omega=\omega_c}. \tag{4}$$

Equivalently, the time delay of a segment of length d inside the bulk material is given by

$$\tau = d/v_g = (d/c)n_g, \tag{5}$$

where

$$n_g = n(\omega) + \omega \frac{\partial n}{\partial \omega}.$$

Clearly the normalized time delay $\tau/(d/c)$ is equivalent to the group index $n_{\rm g}$. We shall use the normalized delay as a measure of the delays in transmission across the RT structure (figure 2).

We start with the permittivity (ϵ) and permeability (μ) from the experimental work of Dolling *et al* [14] for the NIM guide. The data for ϵ and μ have been digitized from their results. Although it is understood that the experimentally reported MMs are highly anisotropic, we assume the NIM to be homogeneous and isotropic for our calculations. The permittivity of the NIM guide is taken to be the same as in the experiment of Dolling *et al*, whereas the magnetic permeability is modelled by a theoretical fit of the experimental data to a Lorentz-type response. We pay special attention to the magnetic response as magnetic losses form the dominant mechanism of losses at higher frequencies. As mentioned earlier, losses in realistic MMs are too high for the RT peaks in transmission to show up and that absorption-compensation forms the basis for the recovery of these resonances. With this goal in mind we dope the MM with a gain material again with Lorentz-type response, albeit with negative oscillator strength. Thus the magnetic response is taken to be

$$\mu(\lambda) = \mu_\infty + \frac{\sigma_1}{1-(\lambda_1/\lambda)^2 - i(\lambda_1/\lambda)\gamma_1} + \frac{f\sigma_2}{1-(\lambda_2/\lambda)^2 - i(\lambda_2/\lambda)\gamma_2}, \quad (6)$$

where the first two terms give a Lorentz-type fit [44] to the magnetic response of the experimental MM [14]. The last term gives the contribution of the gain material (with $\sigma_2 < 0$) to the permeability. The parameter f is a measure of the dopant's density such that at $f = 0$ we recover the experimental material. Hereafter we refer to this material with $f = 0$ as Dolling's material. The parameters $\mu_\infty = 0.6$, $\sigma_1 = 4.425\gamma_1$, $\gamma_1 = 0.028$ and $\lambda_1 = 1.459$ μm are chosen to fit the experimental data of Dolling *et al*. The parameters for the active material are taken to be $\sigma_2 = -0.0054292$, $\gamma_2 = 0.0028$, $\lambda_2 = 1.43642$ μm such that at $f = 1$ the MM is fully absorption-compensated at the working wavelength $\lambda_0 \approx 1.436$ μm (see figure 3).

In what follows we first present the results for the intensity transmission profile of the structure showing the emergence of plasmon-like modes and obtain the corresponding delay features without and with absorption-compensation. We choose the parameters of the layered structure as follows: $\epsilon_i = \epsilon_f = 6.145$, $\epsilon_1 = \epsilon_3 = 2.25$, $\mu_i = \mu_f = \mu_1 = \mu_3 = 1$ and $d_1 = d_3 = 1$ μm, $d_2 = 0.5$ μm for exciting the plasmon-like modes (with TE polarized light). The results for the intensity transmission and the delay (normalized to $d_{\rm T}/c$, $d_{\rm T} = d_1 + d_2 + d_3$) are shown in figures 4a and 4b, respectively. The right-most sharp peak in figure 4a can easily be recognized as a plasmon-like mode, because the refractive index (modulus of the real part) of the NIM slab is lower than that of the dielectric spacer layer, and the corresponding angle of incidence is beyond the total internal reflection angle of both prism–dielectric and dielectric–NIM interfaces. This ensures evanescent waves in both the dielectric and the NIM. Figures 4a and 4b show the results for both Dolling's material and its absorption-compensated equivalent. The transmission for Dolling's material has been scaled up by a factor of 10 for comparison (dashed curve). It is clear that the losses in Dolling's material prohibit the excitation of the plasmon-like modes. Evidently there is no point in talking about delay if almost nothing gets transmitted. Clearly, a compensated absorption (see the solid curves

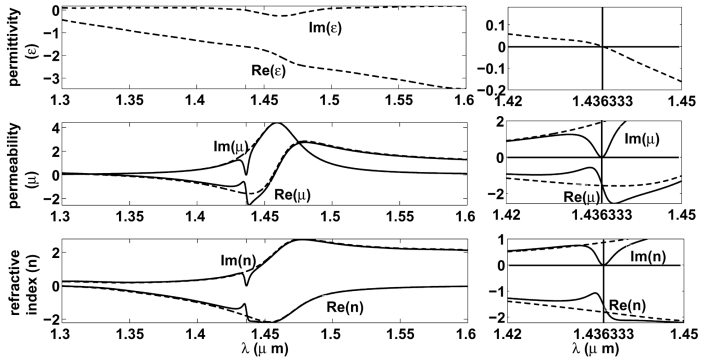

Figure 3. Permittivity ϵ (top), permeability μ (middle) and refractive index n (bottom) as a function of wavelength (λ). Their real and imaginary parts are labelled close to the curves. The dashed (solid) curves correspond to the NIM without (with) doping. The right panels are expanded views of the left panels around $\lambda_0 = 1.436333$ μm (vertical line). The horizontal line marks the zero value on the vertical axis.

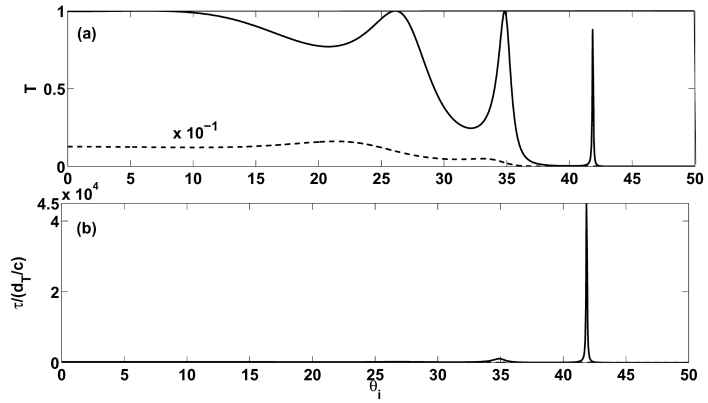

Figure 4. (**a**) Intensity transmission (T) and (**b**) normalized time delay ($\tau/(d_{\rm T}/c)$) with (solid) and without (dashed) absorption-compensation for plasmon-like modes in the NIM guide. The dashed curve in (a) is scaled up by a factor of 10. The parameters for the structure are $\epsilon_i = \epsilon_f = 6.145$, $\epsilon_1 = \epsilon_3 = 2.25$, $\mu_i = \mu_f = \mu_1 = \mu_3 = 1$ and $d_1 = d_3 = 1$ μm, $d_2 = 0.5$ μm.

in figures 4a and 4b) recovers both large transmission and delay. Thus the possibility of large delay in passive MM guides is practically impossible due to large losses, while introduction of gain near the working frequency can render RT as an effective tool for delay devices.

We now look at the guided modes of the layered structure. Such modes can be excited at angles of incidence allowing evanescent waves in the dielectric slabs and propagating waves in the NIM. Thus θ_i must lie between the critical angles for the prism–dielectric and prism–NIM interfaces. We choose the same parameters as before except $\epsilon_1 = \epsilon_3 = 1, d_1 = d_3 = 0.25$ μm and $d_2 = 3$ μm. With Dolling's material these modes may be excited in the range of angles $23.8^\circ < \theta_i < 46.9^\circ$.

The intensity transmission profile (figure 5a) of the structure with the lossy NIM slab (dashed curves) shows that there is practically no transmission through the structure because of large losses in the thicker layer. In contrast, for the absorption-compensated NIM, the guided modes are excited for $23.8^\circ < \theta_i < 38.6^\circ$. The solid curves show intensity transmission (normalized time delays) as functions of θ_i in figure 5a (figure 5b). Note that for the said parameter values, two guided modes are excited, while the transmission peak occurring at $\theta_i < 23.8^\circ$ is identified as the Fabry–Pérot (FP) resonance of the structure. Again, large phase delays are associated with the excited guided modes of the structure in the absorption-compensated NIM.

4. Imaging through an absorption-compensated slab of the metamaterial

In this section we consider another promising application of NIMs that has attracted a lot of attention, namely, perfect imaging. Pendry had shown that a slab of lossless NIM could be used to focus propagating as well as evanescent waves from a source [7]. This implies the perfect reproduction of object details at length scales much beyond the Rayleigh limit. Pendry's lens works by amplifying the evanescent waves in the NIM so that the amplitudes of propagating and evanescent waves are perfectly recovered at the image plane. This has spurred the exploration of SR abilities with current day MMs and other structures (for example, stacks of metal and dielectric [45]) to achieve super-lensing. Extensive experimental and numerical studies have demonstrated the SR abilities of NIMs [46–50]. Experimentally a resolution of $\lambda/8$ was achieved by Aydin *et al* [50] in the microwave domain. The hurdle for 'perfect' imaging can again be traced to the high losses of the current MMs. The resolution limit has a logarithmic dependence on the NIM losses [51,52]. The focal distance of such lossy lenses (also logarithmically dependent on the loss) is comparable to the wavelength and can be advantageous only in the near-field [53,54]. Such lenses are

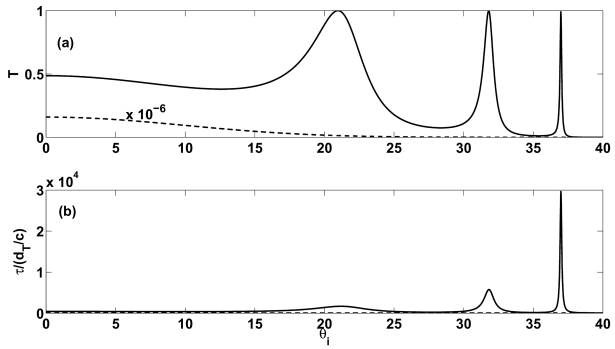

Figure 5. (**a**) Intensity transmission (T) and (**b**) normalized time delay ($\tau/(d_\mathrm{T}/c)$) with (solid) and without (dashed) absorption-compensation for guided modes in the NIM guide. The dashed curve in (a) is scaled up by a factor of 10^6. The parameters for the structure are: $\epsilon_1 = \epsilon_3 = 1$, $d_1 = d_3 = 0.25$ μm and $d_2 = 3$ μm. Other parameters are as in figure 4.

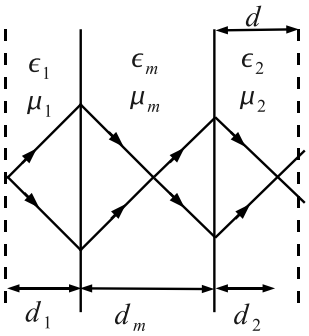

Figure 6. Scheme for imaging using an NIM slab (width d_m and refractive index $n_m = \sqrt{\epsilon_m \mu_m}$). The ambient medium has a refractive index $n_{1(2)} = \sqrt{\epsilon_{1(2)} \mu_{1(2)}}$ on the object (image) side. The object ('perfect' image) plane is at a distance d_1 (d_2) from the NIM slab surface. d is the distance at which the image is observed.

sometimes referred to as near-sighted. Ramakrishna *et al* showed the possibility of improving the resolution of a near-field lens using an alternating stack of gain-doped positive and lossy silver layers [55]. These studies suggest that removal of NIM losses can help in improving the resolution limit and achieving near-perfect imaging.

We now explore the possibility of achieving near-perfect imaging by an absorption-compensated (as in §3) NIM slab. We use the material with permittivity from the results of Dolling *et al* [14] and a permeability modelled by eq. (6). Recall that at $f = 1$ (eq. (6)) the NIM becomes transparent at the free space working wavelength λ_0. An object illuminated by light at this wavelength is placed at a distance d_1 from the interface of an NIM slab (of thickness d_m). The image would then be formed at a distance d_2 from the other interface of the slab (see figure 6). These distances are related (in the paraxial approximation) by [8]

$$d_2 = \frac{n_2}{|n_m|} d_m - \frac{n_2}{n_1} d_1, \tag{7}$$

where n_1 and n_2 are the refractive indices of the ambient media and n_m is that of the NIM slab; d_1 (d_2) is the object ('perfect' image) distance and d_m is the thickness of the NIM slab. In what follows, we work with a symmetric configuration, i.e., $\epsilon_1 = \epsilon_2$, $\mu_1 = \mu_2$. The thickness of the NIM slab is chosen to have a fixed optical width $d_m = 2|n_m|\lambda_0$. Choosing $d_1 = n_1 d_m/(2n_m)$ ensures $d_1 = d_2$ and that the image inside the NIM slab is formed at its centre. To obtain the transmitted field amplitude we first compute the Fourier spectrum of the field amplitude from the illuminated object. The amplitude transmission at the image plane for each spectral component is then computed using the characteristic matrix approach. The amplitude at the image plane is then reconstructed from the transmitted spectrum. We note that the contribution of the evanescent waves (transverse wave number k_x larger than $2\pi n_1/\lambda_0$) along with the propagating waves is accounted by a suitably large spectral domain. We tested our code using a standard Pendry lens configuration, which yielded perfect imaging at the specified image plane. We also looked at the images

in planes before and after the 'perfect' image plane in order to verify the distortions. Effect of small losses is also investigated. We do not present these results and move to the case of lensing with absorption-compensated MMs. We consider two specific cases: (a) when all the media are index-matched and (b) when they are impedance-matched.

Let the transverse field distribution corresponding to the superposition of two Gaussians of width $\lambda_0/10$ and peaks separated by $\lambda_0/5$ (at the working wavelength $\lambda_0 \approx 1.4363$ μm) define our object. An absorption-compensated NIM (discussed in §3) slab is used for the lens. The refractive index of the non-magnetic ambient medium ($\mu_1 = 1$) is matched with the NIM by setting $\epsilon_1 = |\epsilon_2\mu_2/\mu_1|$. The object distance and the slab thickness are chosen for the symmetric configuration as discussed earlier. We image the two adjacent Gaussians at and away from the 'perfect' image plane and plot the intensities in figure 7. The object (solid) is imaged (dashed) at $d = d_2$ with distinguishable peaks, whereas, a significant degradation of images (reduced intensity and broadening) occur at $d = d_2 \pm 0.3\lambda_0$ (almost overlapping dotted and dash-dotted curves). A significant amount of reflection occurs at the NIM interfaces causing a reduction in the image intensity [7,53]. Thus, an absorption-compensated NIM slab placed in a refractive index-matched medium can be used for imaging with sub-wavelength resolution, albeit with reduced intensity.

We now consider the second case, namely, imaging at a wavelength where the NIM is impedance-matched to the ambient medium (free space). Note that such impedance-matching requires $|\mathrm{Re}(\epsilon_m)| = |\mathrm{Re}(\mu_m)|$ leading to finite losses as in the recent experimental studies [48,50]. Near-transparency and impedance-matching with free space could not be achieved simultaneously at the same wavelength. These losses are minimized by using suitable dopant parameters: $f = 0.35605$, $\lambda_2 = 1.43615$ μm and $\gamma_2 = 0.001$ in eq. (6). The other parameters in eq. (6) are retained

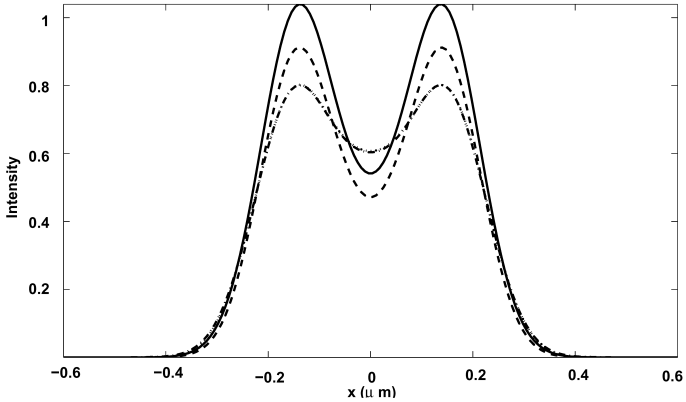

Figure 7. Image intensities with the Pendry scheme at three NIM–to-image plane distances $d = d_2 - 0.3\lambda_0$ (dash-dotted curve), d_2 (dashed curve) and $d_2 + 0.3\lambda_0$ (dotted curve) for an absorption-compensated NIM slab and refractive index-matched ambient medium: $\mathrm{Re}(\epsilon_m(\lambda_0)) = -1.61$, $\mathrm{Re}(\mu_m(\lambda_0)) = -1.48$, $\mu_1 = 1$, $\epsilon_1 = \epsilon_m\mu_m/\mu_1$. Here $\lambda_0 \approx 1.43633$ μm and $d_m = 2n_m\lambda_0$, $d_1 = d_2 = n_1/(2n_m)$. Object intensity (solid curve) is shown for comparison.

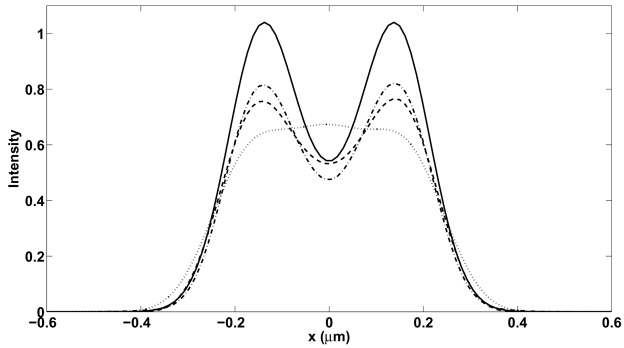

Figure 8. Same as figure 7b but with the NIM slab impedance-matched to free space ($\epsilon_1 = 1,\ \mu_1 = 1$). Images at $d = d_2 - 0.3\lambda_0$ (dash-dotted curve), d_2 (dashed curve) and $d_2 + 0.3\lambda_0$ (dotted curve) and object (solid curve) at $d_1 = d_2$. Here $f = 0.35605$, $\gamma_2 = 0.001$, $\lambda_2 = 1.436315$ μm; other parameters are as in figure 7.

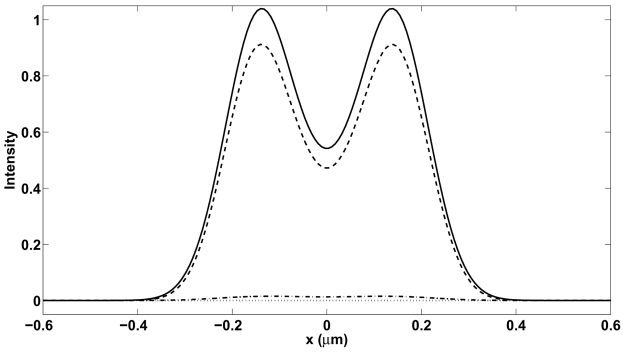

Figure 9. Effect of loss on imaging. Images obtained at the 'perfect' image plane for $f = 1$ (dashed curve), 0.9 (dash-dotted curve) and 0 (dotted curve) compared with the object (solid). Other parameters are same as in figure 7b. Note that for $f = 0$ the curve is flat and near-zero.

as in §3. Figure 8 shows the image intensities formed at $d = d_2$ (dashed curve), $d_2 - 0.3\lambda_0$ (dash-dotted curve) and $d_2 + 0.3\lambda_0$ (dotted curve) along with the object intensity (solid curve). Though the peaks are distinctly imaged, it is clear that the image intensity is degraded in comparison to the index-matched case. It must be noted that although the reflections from the interfaces are absent, the loss within the NIM slab is now larger. Interestingly the imaging is better (see the dash-dot line) for shorter distance from the NIM layer. This is due to the near-sighted nature of a lossy lens [54]. Moreover, this is in contrast with the previous case of mismatched impedance, where the NIM is nearly lossless.

We finally look at the effect of gain in the NIM on the performance of the lens in the index-matched case. We compare the cases $f = 1$ (full absorption-compensation), $f = 0.9$ (partial compensation) and $f = 0$ (Dolling's material). The intensities of the image formed at the 'perfect' image plane for these dopant

densities are shown in figure 9. For $f = 1.0$, the peaks are well-resolved, while for $f = 0.9$ the maximum transmission is about 1.5% and the peaks are difficult to resolve. For the experimental material (without doping) the image intensity is near-zero implying near-null transmission through the structure. Thus, a loss-compensated NIM can again lead to much improved SR applications.

5. Strong interaction between a critically coupled cavity and resonant atoms

In this section we look at yet another recent application of MMs, namely, critical coupling in a cavity with MM mirrors leading to near-perfect absorption. In contrast to the previous sections we will consider MMs in a frequency domain where $\mathrm{Re}(\epsilon) < 0$ and $\mathrm{Re}(\mu) > 0$. Recall that CC implies a near-total suppression of reflection and transmission at one or more frequencies. CC was first demonstrated in a layered structure for normal incidence at a single frequency using a highly absorbing polymer film [56]. Later it was shown that simultaneous CC at distinct frequencies can be achieved in a similar system when the polymer film is replaced by a silver-colloid film [57]. Localized plasmons in the metal colloid film were exploited to this end. Further, these studies were extended to the case of oblique incidence and both types of polarizations TE and TM [58]. CC in such systems occur because of the purely imaginary Poynting vector inside the layered structure [56]. But, the CC frequencies of such structures are restricted by the narrow-band features of the absorbers. A subsequent study of an MM cavity showed the remarkable tunability of the CC frequencies via the angle of incidence [59]. This was achieved through the tunability of Fabry–Pérot (FP) resonances of the cavity by changing its free spectral range. Further, such a cavity, when critically coupled, exhibits a large local field enhancement. Such are the features that are sought for cavity QED studies on strong atom–cavity interaction [60–63]. In a strongly interacting atom–cavity system, due to long-lived photons in the high-finesse cavity, there is a periodic exchange of energy between the atom and the cavity mode. This results in a frequency and life-time splitting of the coupled system. Thus strong atom–field coupling in the context of a critically coupled cavity is of fundamental interest and was studied in detail recently [29]. Here we recall the basic features of such an interaction.

We consider a cavity formed by sandwiching a dielectric layer between two MM slabs (see figure 10) and recall the results of doping the cavity with atoms resonant at the CC frequency [29]. To begin with, we list out the properties of an MM slab necessary for forming the mirrors of the FP cavity (as in figure 10). Again we use a Lorentz-type response for the MM expressed in a slightly different form [64]

$$\epsilon(f) = 1 - \frac{f_{\mathrm{ep}}^2 - f_{\mathrm{eo}}^2}{f^2 - f_{\mathrm{eo}}^2 + i\gamma f},$$
$$\mu(f) = 1 - \frac{f_{\mathrm{mp}}^2 - f_{\mathrm{mo}}^2}{f^2 - f_{\mathrm{mo}}^2 + i\gamma f}, \tag{8}$$

where f_{ep} (f_{mp}) is the electric (magnetic) plasma frequency, f_{eo} (f_{mo}) is the electric (magnetic) resonance frequency and γ is the decay rate (assuming the same

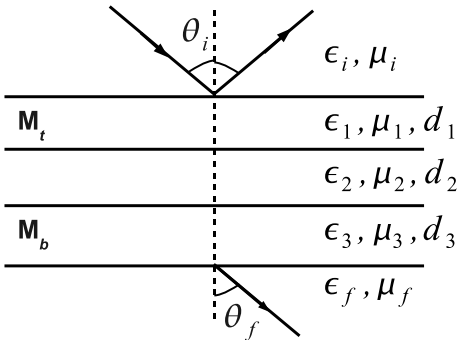

Figure 10. Schematic of the layered structure for CC with a dielectric layer of thickness d_2 sandwiched between two MM layers M_t and M_b.

decay rate for both electric and magnetic resonances). Subsequently, Bloemer *et al* [24] investigated the frequency domain between the electric and magnetic plasma frequencies and showed that the MMs exhibit an omnidirectional band gap (much like in 1D photonic band gap (PBG) structures). The stop gap in MMs arise from the nearly imaginary refractive index (a consequence of the opposite signs of $\mathrm{Re}(\epsilon)$ and $\mathrm{Re}(\mu)$) prohibiting propagating wave solutions in the NIM. In contrast, the band gap in PBG structures originate from the constructive interference of smaller reflections at the periodically arranged interfaces. The plasma frequencies (and thereby the stop band) of the MMs are controllable via the filling fraction of the wire and split ring structures of the MM unit cell [2,65]. Bloemer *et al* [24] had assumed that the MM is 3D isotropic and homogeneous. We used such a slab with the same parameters as in [24] for the bottom MM layer (M_b) (see figure 10). The plasma frequencies of the top MM slab (M_t) were chosen such that its stop gap lies well within that of M_b. Thus the parameters for M_b are: $f_{ep} = 12.8$ GHz, $f_{mp} = 10.95$ GHz, $f_{mo} = 10.05$ GHz, $f_{eo} = 10.3$ GHz, $\gamma = 0.01$ GHz and $d_3 = 15$ cm. For M_t the parameters are the same, except for $f_{ep} = 11.75$ GHz, $f_{mp} = 11.4$ GHz and $d_1 = 9$ cm. It is to be noted that the transmission across the structure is prevented by the broadband reflection of M_b. An interplay of the FP resonances of the cavity (formed by the suitably thick dielectric layer) with the band-edge features of M_t results in a complete absorption of the incident radiation (at a particular frequency) in the structure. The CC frequency was shown to be tunable by merely changing the angle of incidence. Further, CC was also achieved simultaneously at another frequency by changing the spacer layer thickness (d_2) in discrete steps. The step size ensured that the phase change in the dielectric for the already critically coupled frequency was in multiples of 2π [59].

We consider the parameters of the above structure critically coupled at normal incidence near the electric plasma frequency of M_t, namely, $\epsilon_2 = 3.8$, $\mu_2 = 1$, $d_2 = 21.126$ cm, $d_1 = 9$ cm and $d_3 = 15$ cm. The total scattering $(R + T)$ and the intensity transmission from the structure are shown in figure 11. Doping the dielectric layer with atoms close to the CC frequency, expectedly, results in splitting of the CC resonace dip as in the usual vacuum field Rabi splitting [25–28]. Such normal mode splittings were studied in detail in the context of FP, modulated FP and spherical cavities (supporting whispering gallery modes) [33,66–68]. For the

structure in figure 10 with a doped cavity, we recall the total scattering results computed using the characteristic matrix approach. The permittivity of the non-magnetic ($\mu_2 = 1$) doped dielectric layer is taken as

$$\epsilon_2(f) = \epsilon_{\rm h} + \frac{f_p^2}{f_{02}^2 - f^2 - i\gamma_2 f} \ , \tag{9}$$

where $\epsilon_{\rm h}$ is the dielectric constant of the host material, f_p^2 is proportional to the dopant density, f_{02} and γ_2 are the resonance frequency and the decay rate of the atom, respectively. Recall that the atom is assumed to be near-resonant to the CC frequency of the undoped cavity. The splitting of the CC resonance at two dopant densities is shown in figure 12 (for $\gamma_2 = 0.0008$). It is clear that the separation of the split modes increases with increasing dopant density. Further, the split mode at the higher (lower) frequency becomes wider (narrower) with increasing f_p. At a sufficiently large f_p the total scattering of the higher frequency split mode reaches near-zero, again resulting in CC.

These observations can be confirmed from the analysis of the roots of the dispersion relation (eq. (3)). Note that eq. (3) is transcendental and admits solutions

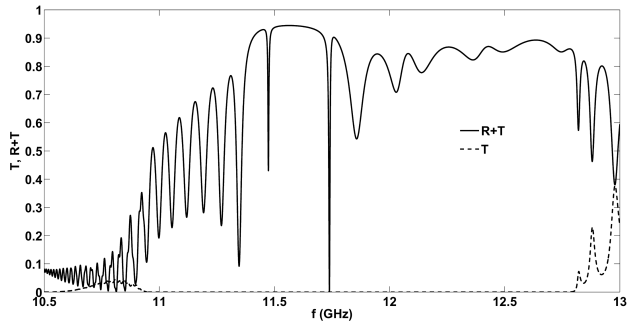

Figure 11. CC near the electric plasma frequency of $\rm M_t$ for normal incidence. $\epsilon_2 = 3.8$, $\mu_2 = 1$, $d_2 = 21.126$ cm, $d_1 = 9$ cm and $d_3 = 15$ cm.

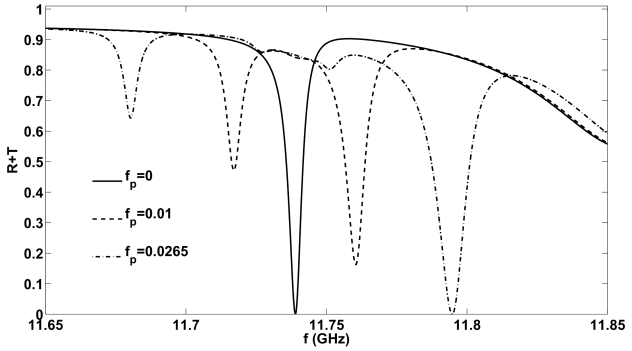

Figure 12. Split resonances for the dopant densities $f_p = 0.01$ (dashed curve) and 0.0265 (dash-dotted curve). Here $\gamma_2 = 0.0008$. The curve for $f_p = 0$ (solid curve) is produced for reference. Other parameters are the same as in figure 11.

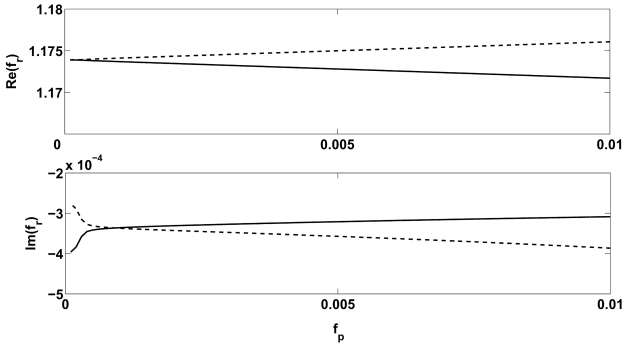

Figure 13. The real (top) and imaginary (bottom) parts of the roots of the dispersion relation (f_r) of the layered structure as a function of the atomic density at $\gamma_2 = 0.0008$. The solid (dashed) curve corresponds to the split resonance at the lower (higher) split frequency.

(f_r) only for complex frequencies. Recall that the real part (absolute value of the imaginary part) of f_r carries the information about the location (width) of the split modes. The solution of the dispersion relation as a function of f_p is shown in figure 13. The high (low) frequency split mode is marked by dashed (solid) lines. The real part of the roots of eq. (3) show the increasing separation of the split modes (top panel, figure 13). The imaginary parts (absolute value) of f_r confirm the widening (narrowing) of the high (low) frequency split modes. This is in conformity with the earlier total scattering results.

6. Conclusions

We have considered three potential device applications of MMs considering their absorption and dispersion in the framework of a full causal response. We showed how in current realizations of MMs, the losses wash out the interesting transmission and delay features in RT. Perfect imaging abilities of current day passive metamaterials are also limited due to their intrinsic losses. Absorption-compensation by introducing gain was explored as a possible route to overcome these limitations. The possibility of achieving large transmission delays was also shown. Absorption-compensation proved to be useful in the context of perfect imaging also. Introduction of gain in the magnetic response is shown as a possible route to realize such devices. Finally, strong atom–cavity interaction in a doped FP cavity with MM mirrors was studied to show the normal mode splittings.

Acknowledgements

The authors are thankful to the Department of Science and Technology, Govt. of India for supporting this work. One of the authors (S Dutta Gupta) is thankful to the Nano Initiative Program, University of Hyderabad for partial support.

References

[1] V G Veselago, *Sov. Phys. Uspekhi* **10**, 509 (1968)
[2] J B Pendry, A Holden, D Robbins and W Stewart, *IEEE Trans. Microwave Theory Tech.* **47**, 2075 (1999)
[3] S A Ramakrishna, *Rep. Prog. Phys.* **68**, 449 (2005)
[4] D R Smith, W J Padilla, D C Vier, S C Nemat-Nasser and S Schultz, *Phys. Rev. Lett.* **84**, 4184 (2000)
[5] V M Shalaev, *Nature Photon.* **1**, 41 (2007)
[6] J B Pendry, *Contemp. Phys.* **45**, 191 (2004)
[7] J B Pendry, *Phys. Rev. Lett.* **85**, 3966 (2000)
[8] N Fang and X Zhang, *Appl. Phys. Lett.* **82**, 161 (2003)
[9] N I Zheludev, S L Prosvirnin, N Papasimakis and V A Fedotov, *Nature Photon.* **2**, 351 (2008)
[10] N Engheta, *Science* **317**, 1698 (2007)
[11] S Dutta Gupta, R Arun and G S Agarwal, *Phys. Rev.* **B69**, 113104 (2004)
[12] N Papasimakis, V A Fedotov, N I Zheludev and S L Prosvirnin, *Phys. Rev. Lett.* **101**, 253903 (2008)
[13] C Caloz and T Itoh, *Electromagnetic MMs: Transmission line theory and microwave applications* (John Wiley & Sons Inc., New Jersey, 2006)
[14] G Dolling, C Enkrich, M Wegener, C M Soukoulis and S Linden, *Opt. Lett.* **31**, 1800 (2006)
[15] E P Wigner, *Phys. Rev.* **98**, 145 (1955)
[16] M I Stockman, *Phys. Rev. Lett.* **98**, 177404 (2007)
[17] P Kinsler and M W McCall, *Phys. Rev. Lett.* **101**, 167401 (2008)
[18] A Degiron, J J Mock and D R Smith, *Opt. Exp.* **15**, 1115 (2007)
[19] P P Orth, J Evers and C H Keitel, arXiv:0711.0303v1 [quant-ph]
[20] V Anant, A F Abouraddy and K K Berggren, arXiv:0711.5021v1 [physics.optics]
[21] S Chakrabarti, S A Ramakrishna and H Wanare, *Opt. Lett.* **34**, 3728 (2009)
[22] Y Sivan, S Xiao, U K Chettiar, A V Kildishev and V M Shalaev, *Opt. Exp.* **17**, 24060 (2009)
[23] Y Zeng, Q Wu and D H Werner, *Opt. Lett.* **35**, 1431 (2010)
[24] M Bloemer, G D'Aguanno and M Scalora, *Appl. Phys. Lett.* **87**, 261921 (2005)
[25] M G Raizen, R J Thompson, R J Brecha, H J Kimble and H J Carmichael, *Phys. Rev. Lett.* **63**, 240 (1989)
[26] R J Thompson, G Rempe and H J Kimble, *Phys. Rev. Lett.* **68**, 1132 (1992)
[27] H J Carmichael, L Tian and W Ren, *Advances in atomic, molecular and optical physics*, supplement 2 edited by P R Berman (Academic Press, Boston, 1994)
[28] D Sarid, *Phys. Rev. Lett.* **47**, 1927 (1981)
D Sarid, *Phys. Rev. Lett.* **48**, 446 (1982)
[29] S Dutta Gupta, S Deb and S Dutta Gupta, *J. Opt.* **12**, 075103 (2010)
[30] M Born and E Wolf, *Principles of optics: Electromagnetic theory of propagation* (Cambridge University Press, Cambridge, 2003)
[31] P Yeh, *Optical waves in layered media* (Wiley, New York, 1988)
[32] S Dutta Gupta, Progress in optics, in: *Nonlinear optics of stratified media* edited by E Wolf (Elsevier Science, Amsterdam, 1998) Vol. 38
[33] S Dutta Gupta and G S Agarwal, *Opt. Comm.* **103**, 122 (1993)
[34] I Newton, *Opticks or a treatise of the reflections, refractions, inflections, and colours of light* (Dover Publications, New York, 1952)
[35] R Y Chiao, P G Kwait and A M Steinberg, *Physica* **B175**, 257 (1991)

[36] H Mizuta and T Tanoue, *The physics and application of resonant tunneling diodes* (Cambridge University Press, Cambridge, 1995)
[37] R Dragila, B Luther-Davies and S Vukovic, *Phys. Rev. Lett.* **55**, 1117 (1985)
[38] Ivan Avrutsky, Yang Zhao and Vladimir Kochergin, *Opt. Lett.* **25**, 595 (2000)
[39] S Tomita *et al*, *Opt. Exp.* **16**, 9942 (2008)
[40] Sergei Sidorenko and Olivier J F Martin, *Opt. Exp.* **15**, 6380 (2007)
[41] S Dutta Gupta, *Pramana – J. Phys.* **72**, 303 (2009)
[42] D Golla, S Deb and S Dutta Gupta, arXiv:0911.5374v2 [physics.optics]
[43] Bae-Ian Wu, T M Grzegorczyk, Y Zhang and J A Kong, *J. Appl. Phys.* **93**, 9386 (2003)
[44] S Zhang, W Fan, K J Malloy, S R J Brueck, N C Panoiu and R M Osgood, *Opt. Exp.* **13**, 4922 (2005)
[45] J B Pendry and S Anantha Ramakrishna, *Physica* **B338**, 329 (2003)
[46] J D Baena, L Jelinek, R Marqués and F Medina, *Phys. Rev.* **B72**, 075116 (2005)
[47] A N Lagarkov and V N Kissel, *Phys. Rev. Lett.* **92**, 077401 (2004)
[48] A Grbic and G V Eleftheriades, *Phys. Rev. Lett.* **92**, 117403 (2004)
[49] M W Feise and Y S Kivshar, *Phys. Lett.* **A334**, 326 (2005)
[50] K Aydin, I Bulu and E Ozbay, *Appl. Phys. Lett.* **90**, 254102 (2007)
[51] D R Smith, D Schurig, M Rosenbluth, S Schultz, S A Ramakrishna and J B Pendry, *Appl. Phys. Lett.* **82**, 1506 (2003)
[52] R Merlin, *Appl. Phys. Lett.* **84**, 1290 (2004)
[53] V Veselago, *Appl. Phys.* **B81**, 403 (2005)
[54] V A Podolskiy and E E Narimanov, *Opt. Lett.* **30**, 75 (2005)
[55] S A Ramakrishna and J B Pendry, *Phys. Rev.* **B67**, 201101(R) (2003)
[56] J R Tischler, M S Bradley and V Bulović, *Opt. Lett.* **31**, 2045 (2006)
[57] S Dutta Gupta, *Opt. Lett.* **32**, 1483 (2007)
[58] S Deb, S Dutta Gupta, J Banerji and S Dutta Gupta, *J. Opt. A: Pure Appl. Opt.* **9**, 555 (2007)
[59] S Deb and S Dutta Gupta, *CC in a system of two coupled negative index medium layers*, arXiv:0912.0575v1 [physics.optics] (2009)
[60] S Haroche, Fundamental systems in quantum optics, in: *Cavity quantum electrodynamics* edited by J Dalibard, J M Raimond and J Zinn-Justin (Elsevier Science, 1992)
[61] J R Tischler, M S Bradley, V Bulović, J H Song and A Nurmikko, *Phys. Rev. Lett.* **95**, 036401 (2005)
[62] M G Raizen, R J Thompson, R J Brecha, H J Kimble and H J Carmichael, *Phys. Rev. Lett.* **63**, 240 (1989)
[63] R J Thompson, G Rempe and H J Kimble, *Phys. Rev. Lett.* **68**, 1132 (1992)
[64] R A Shelby, D R Smith and S Schultz, *Science* **292**, 77 (2001)
[65] R A Shelby, D R Smith, S C Nemat-Nasser and S Schultz, *Appl. Phys. Lett.* **78**, 489 (2001)
[66] V S C Manga Rao, S Dutta Gupta and G S Agarwal, *Opt. Lett.* **29**, 307 (2004)
[67] G S Agarwal and S Dutta Gupta, *Opt. Comm.* **93**, 173 (1992)
[68] S Dutta Gupta and G S Agarwal, *Opt. Comm.* **115**, 597 (1995)